Конференция «The Role of Gas in Galaxy Dynamics»

October 2-6, 2017 – Valletta, Malta

Конференция в цифре:

- 140 участников;
- 2 пленарных доклада – от F. Combes и J. Bland-Hawthorn, по 45 минут;
- «приглашенные доклады» по 30 минут: Bigiel, Carollo, Schinnerer, Fraternali, Fox, Renault, Hunt, Lilly, summary by Ken Freeman;
- Куча устных докладов по 15 минут, около 50 постеров.

Knapen:

- WEAVE at the WHT→ 2019?;
- IFU modes: `small IFU', 11''x12'', 20 together, spaxel 1.3''
- `Large IFU': field 1.3'x1.5', spaxel 2.6'', range 3000-7500 A (two arms), spectral resolution 5700. →
- Galaxy survey! 225 targets, exposures up to 10h, PI J. Falcon-Barroso

Debattista

- Wang+2008: красные галактики со-осны со своими гало, спиральные ориентируют диски случайным образом;
- У нашей Галактики триаксиальное гало: 1:0.95:0.72, а спин вроде бы направлен вдоль промежуточной оси. Неустойчивая конфигурация. Но.. См. 1й пункт.
- Earp+2017: Milky Way аккрецирует НАКЛОННЫЙ поток; ожидается поворот плоскости диска с темпом 6.3 градуса за миллиард лет. Доступно GAIA!

HVC in Milky Way: источник аккреции?

- Fox: COS/HST, SII1206 absorption lines, 40% покрытие «неба» Галактики, темп аккреции на диск Галактики 0.4-1.4 масс Солнца/год.
- SFR (Milky Way)=1.9 масс Солнца/год;
- А вот Магелланов Поток дает 4-7 масс Солнца в год!
- Pardy: модель Besla для Магелланова Потока (что это газ SMC) не проходит – не получается ионизованный компонент. И почему в Потоке больше газа (2 млрд солнечных масс), чем осталось в Облаках?? Это не грав. прилив!
- Di Teodoro: А в центре Галактики HVC прекрасно укладываются в конструкцию ветра – скорость ветра 300-400 км/с, угол раствора конуса больше 140 градусов.

Ветра (фонтаны) и аккреция:

- I-Ting Ho: первый релиз SAMI – 800 галактик. Из низ выбрали 40 edge-on. Круглые поля скоростей! Много газа вне плоскости. Ветра начинаются с пов. Плотности SFR log~-2.7. Есть плоскопараллельные геометрии, есть конуса.
- Pezzulli: со ссылкой на Zheng+17, в M33 видна аккреция по всему диску. Предлагается (вместе с Фратернали) модель аккреции из горячей короны, У КОТОРОЙ СКОРОСТЬ ВРАЩЕНИЯ 70%-80% ОТ СКОРОСТИ ВРАЩЕНИЯ ДИСКА. Тогда будут радиальные потоки газа, и получится градиент металличности.

Kassin: эволюция «динамической холодности»

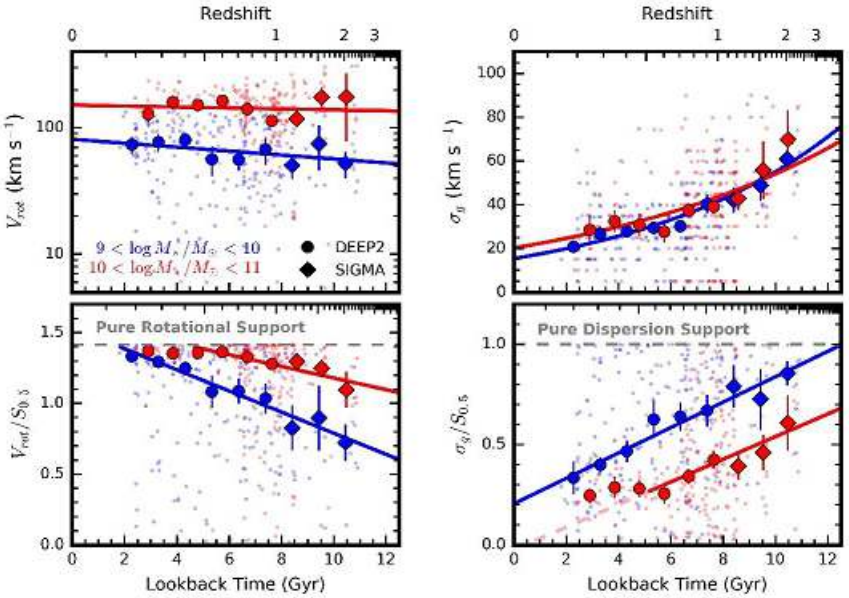

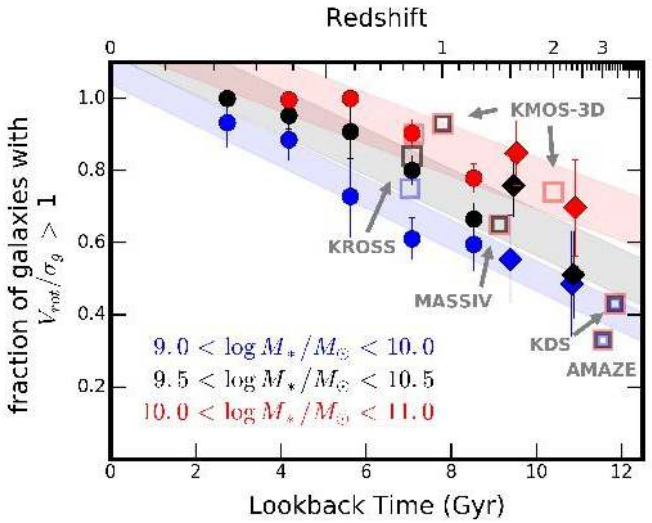

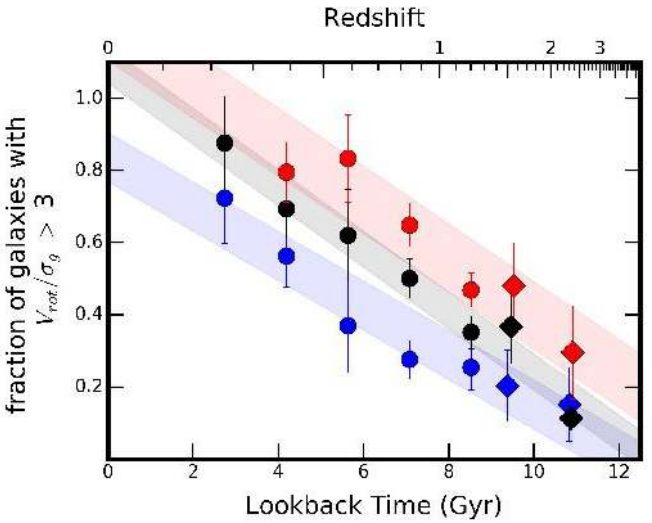

Kassin: эволюция «холодности»

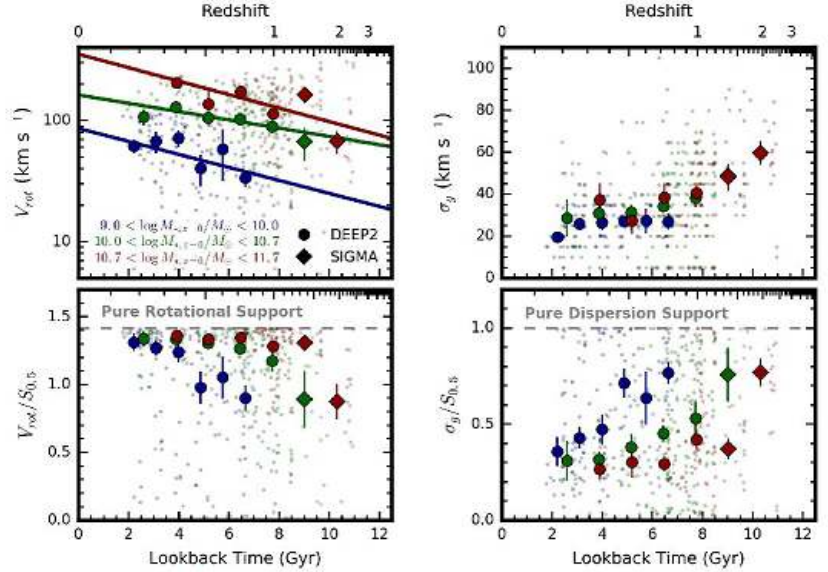

FIG. 6.— The same as Figure 2, but for galaxy populations linked in time via abundance matching. All galaxy populations on average spin-up with time and decrease in disordered motions, i.e., increase in V_{rot} and decline in σ_g. High mass galaxies reach strong levels of rotational support, i.e., $V_{rot}/S_{0.5} > 1.3$ and $\sigma_g/S_{0.5} < 0.4$, by $z = 1.5$ on average. Low and intermediate mass galaxies reach similar levels of rotational support several Gyrs later. The color scheme is the same as in Figure 5 with dark blue, green and red representing the low ($\log M_{*,z=0}/M_\odot \sim 9.4$), intermediate ($\log M_{*,z=0}/M_\odot \sim 10.3$) and high ($\log M_{*,z=0}/M_\odot \sim 11.1$) mass abundance matched populations, respectively. The small points are individual galaxies and large points are the medians in bins of lookback time. The lines are the best-fit relations to the median points of each mass bin.

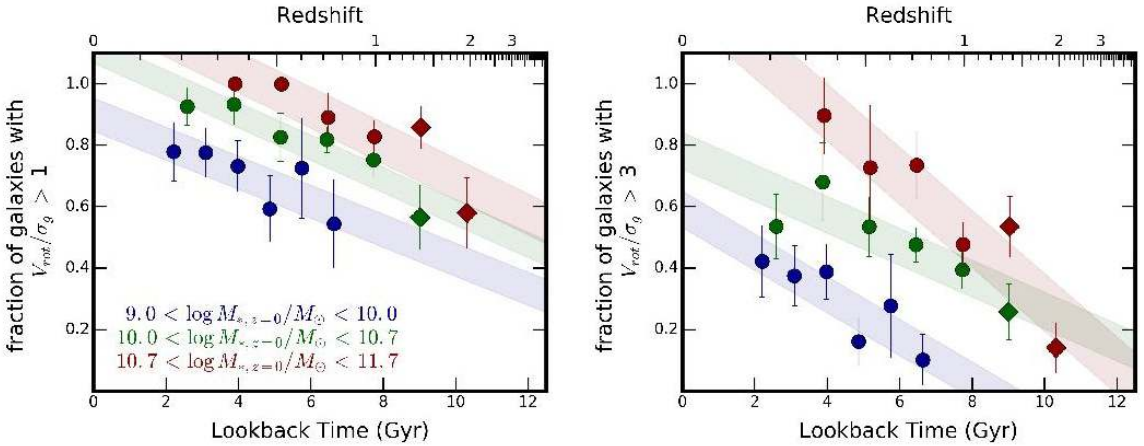

FIG. 8.— The same as Figure 4, but for galaxy populations linked in time via abundance matching. For all three galaxy populations (low, intermediate and high mass), the fractions of galaxies with $V_{rot}/\sigma_g > 1$ and 3 increase significantly with time. At any point in time, higher mass populations have a higher fraction of galaxies meeting these criteria. The fraction of galaxies with $V_{rot}/\sigma_g > 3$ drops below 30% at $z \sim 0.4$ for the low mass galaxy population (blue) and at $z \sim 1.5$ for the more massive galaxy populations (green and red). As in Figure 4, the solid points show measurements from DEEP2 (circles) and SIGMA (diamonds), and the error bars are from bootstrap resampling. The shaded swaths represent the uncertainty on the intercept in a linear fit to the points.

ILLUSTRIS-TNG ("The Next Generation)

Illustris	Model features	TNG	Technical Reference
	MHD		
no	magnetohydrodynamics (MHD)	yes: Powell $\nabla \cdot B$ cleaning	Pakmor, Bauer & Springel 2011
-	Seed B field strength	1.6×10^{-10} phys Gauss at $z = 127$	Pakmor & Springel 2013
-	Seed B field configuration	uniform in random direction	Pakmor & Springel 2013
	BHs and BH Feedback		
$1 \times 10^5 h^{-1}\mathrm{M}_\odot$	BH Seed Mass	$8 \times 10^5 h^{-1}\mathrm{M}_\odot$	Weinberger et al. 2017
$5 \times 10^{10} h^{-1}\mathrm{M}_\odot$	FoF Halo Mass for BH seeding	$5 \times 10^{10} h^{-1}\mathrm{M}_\odot$	Vogelsberger et al. 2013
$\alpha = 100$ Boosted Bondi-Hoyle	BH Accretion	Un-boosted Bondi-Hoyle (w/ v_A)	Weinberger et al. 2017
parent gas cell, Eddington limited	BH Accretion	nearby cells, Eddington limited	Weinberger et al. 2017
fixed to halo potential minimum	BH Positioning	fixed to halo potential minimum	Vogelsberger et al. 2013
Two: "Quasar/Radio"	BH Feedback Modes	Two: "High/Low Accretion State"	Weinberger et al. 2017
Thermal Injection around BHs	High-Accr-Rate Feedback	Thermal Injection around BHs	Weinberger et al. 2017
Thermal 'Bubbles' in the ICM	Low-Accr-Rate Feedback	BH-driven kinetic wind	Weinberger et al. 2017
constant: 0.05	Low/High Accretion Transition: χ	BH-mass dependent, $\leqslant 0.1$	Weinberger et al. 2017
0.2	Radiative efficiency: ϵ_r	0.2	Weinberger et al. 2017
$\epsilon_f \epsilon_r$, with $\epsilon_f = 0.05$	High-Accr-Rate Feedback Factor	$\epsilon_f \epsilon_r$, with $\epsilon_f = 0.1$	Weinberger et al. 2017
$\epsilon_m \epsilon_r$, with $\epsilon_m = 0.35$	Low-Accr-Rate Feedback Factor	$\epsilon_{\mathrm{f,kin}} \leqslant 0.2$	Weinberger et al. 2017
yes	Radiative BH Feedback	yes	Vogelsberger et al. 2013

ILLUSTRIS-TNG ("The Next Generation)

Illustris	Model features	TNG	Technical Reference
	Galactic Winds		
non local, from sf-ing gas	General Approach	non local, from sf-ing gas	Vogelsberger et al. 2013
bipolar	Directionality	isotropic	this paper
cold	Thermal Content	warm	this paper
$\propto$ local $\sigma_{\rm DM}$	Injection Velocity	$\propto$ local $\sigma_{\rm DM}$ with $H(z)$ scaling	this paper
-	Injection Mass Loading	gas-metallicity (Z) dependent	this paper
no	Injection Velocity Floor	yes: 350 $\rm km\,s^{-1}$	this paper
3.7	Wind Velocity Factor: κ_w	7.4	this paper
1.09	Wind Energy Factor: $\bar{e}_w$	3.6	this paper
-	Thermal Fraction: τ_w	0.1	this paper
-	Z-dependence Reduction Factor: $\rm f_{w,Z}$	0.25	this paper
-	Z-dependence Reference Metallicity: $Z_{w,Z}$	0.002	this paper
-	Z-dependence Reduction Power: $\gamma_{w,Z}$	2	this paper
0.4	Metal loading of wind particles: γ_w	0.4	Vogelsberger et al. 2013

ILLUSTRIS-TNG ("The Next Generation)

Illustris	Model features	TNG	Technical Reference
	Stellar Evolution		
Chabrier 2003	IMF	Chabrier 2003	Vogelsberger et al. 2013
$[6, 100]$ $M_\odot$	[min, max] SNII Mass	$[8, 100]$ $M_\odot$	this paper
see Table 2	Yield Tables	see Table 2	this paper
at every star timestep	ISM Chemical Enrichment	time/stellar mass discrete	this paper
	Metal Advection		
gradient extrapolation	Advection Scheme	same + renormalization	this paper
0	Initialization Metal Fractions	10^{-10} at $z = 127$	this paper
H, He, C, N, O, Ne, Mg, Si, Fe	Tracked Element Scalars	same 9 + other metals	this paper
-	Metal Tagging	from SNIa, SNII, AGB separately	Naiman et al. in prep
-	Iron Tagging	from SNIa and SNII separately	Naiman et al. in prep
-	r-processes	from NS-NS mergers	Naiman et al. in prep

ILLUSTRIS-TNG ("The Next Generation)

	Illustris Tables	TNG Tables
AGB	Karakas (2010) $[1-6]\ \mathrm{M}_{\odot}, Z \in [0.0001, 0.004, 0.008, 0.02]$	Karakas (2010) $[1-6]\ \mathrm{M}_{\odot}, Z \in [0.0001, 0.004, 0.008, 0.02]$ Doherty et al. (2014) $[7.0, 7.5]\ \mathrm{M}_{\odot}, Z \in [0.004, 0.008, 0.02]$ Fishlock et al. (2014) $[7.0]\ \mathrm{M}_{\odot}, Z \in [0.001]$
SNII	Portinari, Chiosi & Bressan (1998) $[6-120]\ \mathrm{M}_{\odot}, Z \in [0.0004, 0.004, 0.008, 0.02, 0.05]$	Kobayashi et al. (2006) $[13-40]\ \mathrm{M}_{\odot}, Z \in [0, 0.001, 0.004, 0.02]$ Portinari, Chiosi & Bressan (1998) $[6-13, 40-120]\ \mathrm{M}_{\odot}, Z \in [0.0004, 0.004, 0.008, 0.02, 0.05]$
SNIa	Travaglio et al. (2004) Thielemann et al. (2003)	Nomoto et al. (1997), W7

Table 2. Overview of the choices for the stellar yield tables compiled from the literature in the Illustris versus the TNG model. In the new model, the minimum mass for SNII is raised to $8\mathrm{M}_{\odot}$. To simultaneously use the yields proposed by Kobayashi et al 2006 and Portinari et al. 1998, SNII yields are renormalized such that the IMF-weighted yield ratios at each metallicity are equal to those from the Kobayashi mass range models alone (see text for details).

Успехи IllustrisTNG

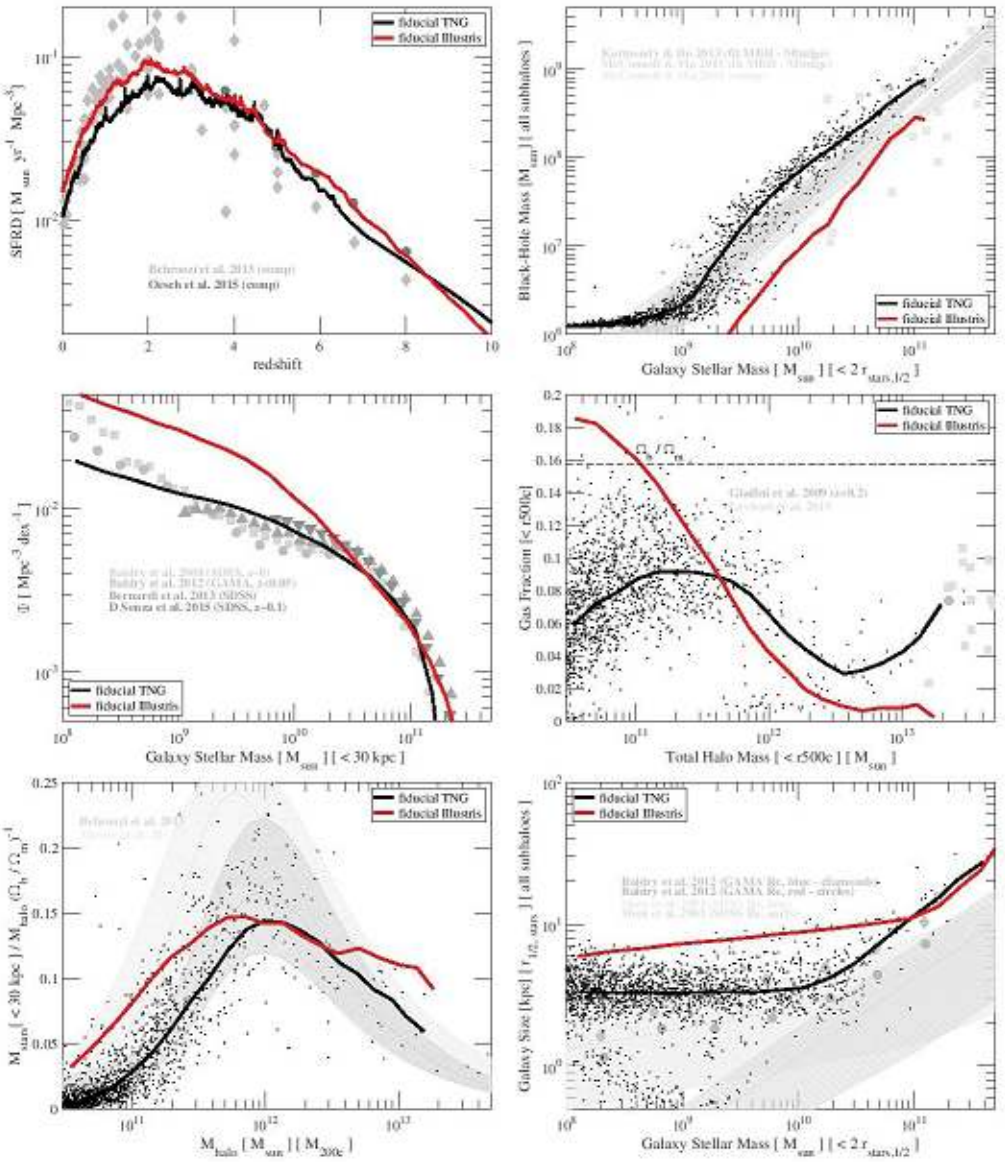

Figure 4. Quantitative properties of the fiducial model via galaxy population statistics at $z = 0$ (unless otherwise stated). The black line shows the result of the fiducial TNG L25n512 simulation, while the red line shows the original Illustris model outcome on the same volume. We always give running medians

Успехи IllustrisTNG

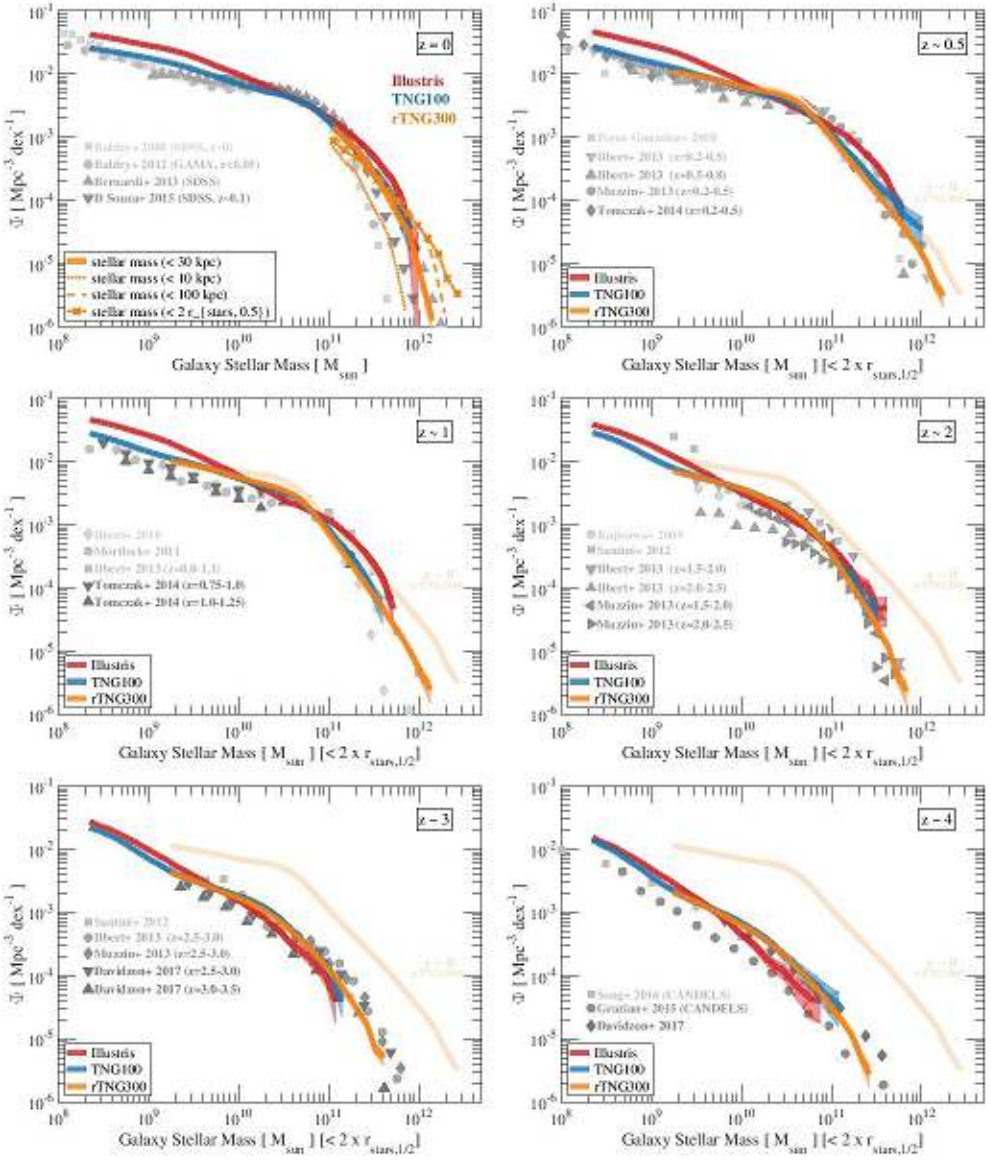

Успехи IllustrisTNG: скучивание

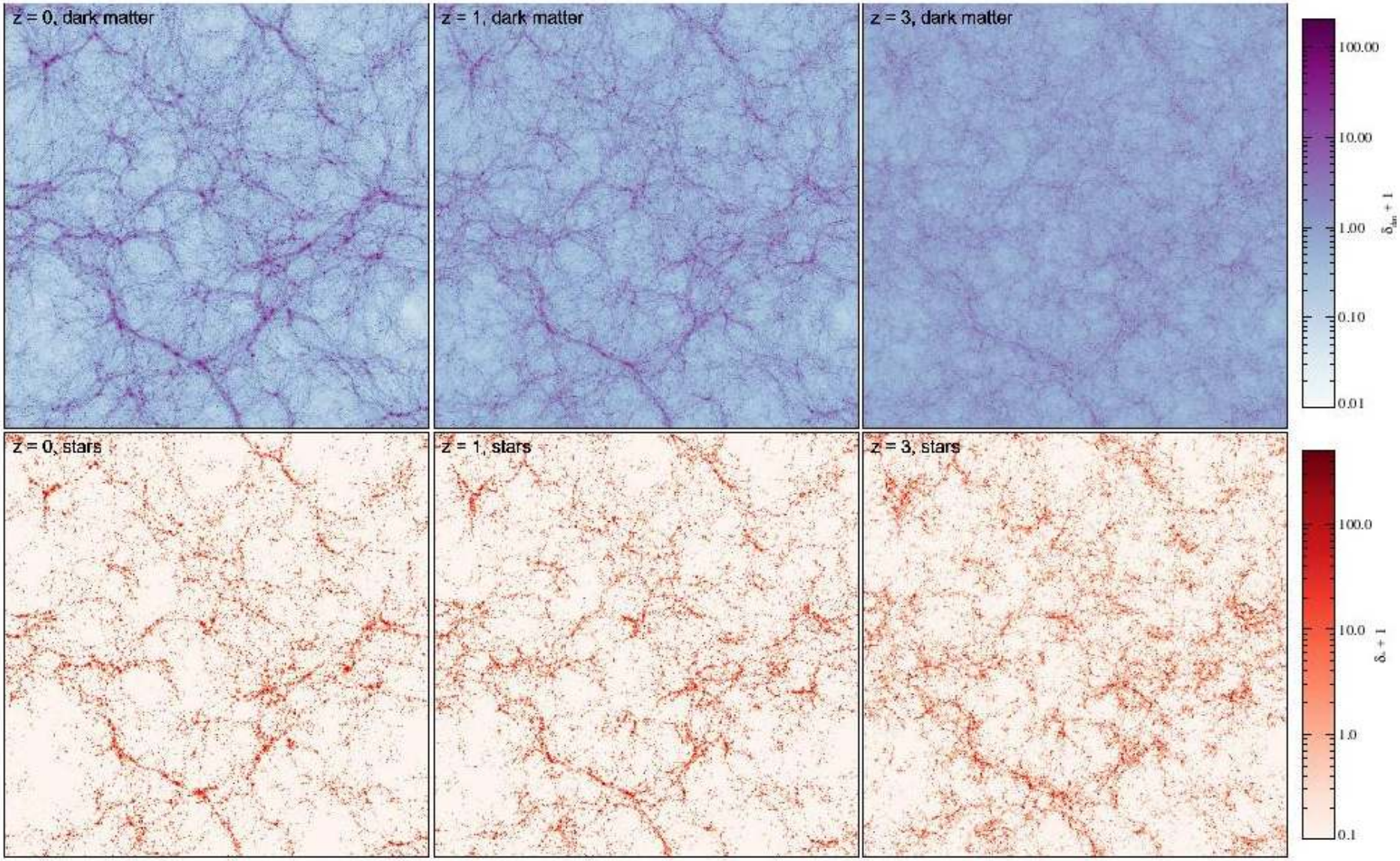

Успехи IllustrisTNG: скучивание

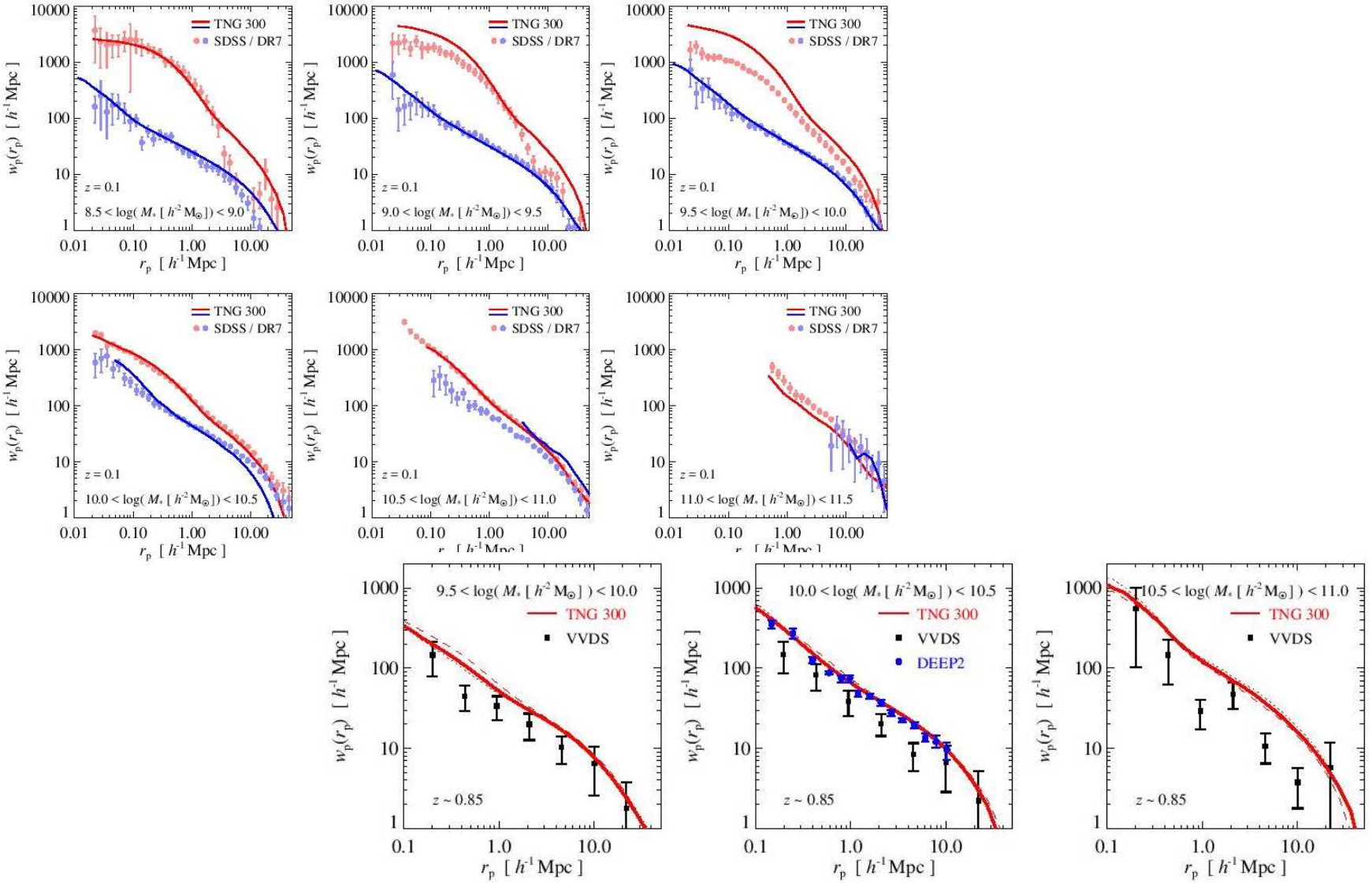

Figure 12. Projected galaxy correlation function of TNG300 in different stellar mass ranges at $z = 0.85$ (solid thick lines), compared to data from the VIMOS VLT Deep Survey (VVDS, Meneux et al. 2008) and from the DEEP2 galaxy redshift survey (Mostek et al. 2013). The VVDS survey covers an extended redshift range, $0.5 < z < 1.2$, and we compare to the simulation results at the midpoint of this interval. To give an illustration of the very small variation of the simulation predictions over this time span, we also include TNG300 results for redshifts $z = 0.5$ (dotted) and $z = 1.2$ (dashed). The DEEP2 results are for a characteristic redshift $z \simeq 0.9$ and refer to an essentially complete sample of galaxies with $\log(M_\star/[h^{-2}M_\odot]) > 10.16$.

Успехи IllustrisTNG: скучивание

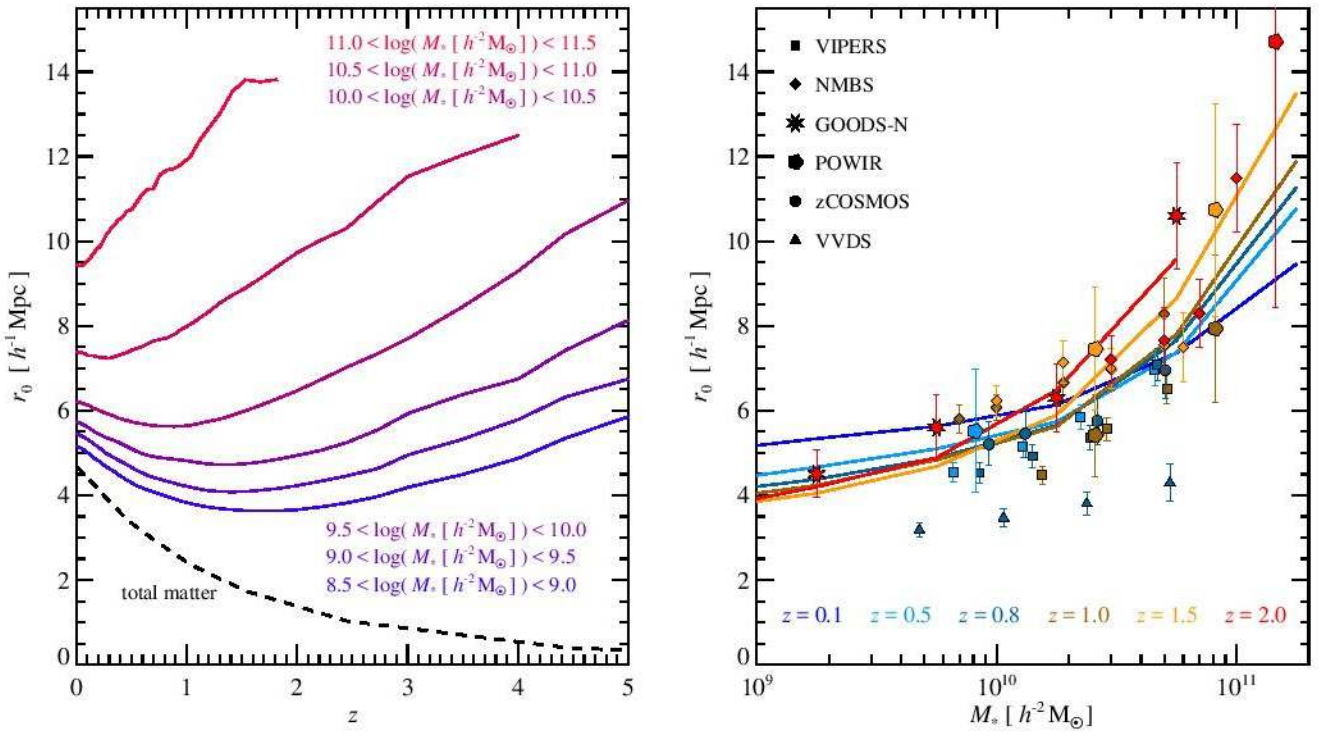

Figure 13. *Left panel:* Clustering length for different galaxy samples from the TNG300 simulation as a function of redshift. We show results for six different stellar mass ranges (coloured lines, as labelled). In each case, we define the clustering length as the scale where the real-space correlation function reaches unity, i.e. $\xi(r_0) = 1$. Deriving this through power-law fits to the real-space or projected correlation function over a range $5\,h^{-1}$Mpc $< r < 20\,h^{-1}$Mpc gives very similar results. We also include the evolution of the correlation length of the total matter correlation function (dashed), which monotonically declines towards

Успехи IllustrisTNG: бимодальность цвета

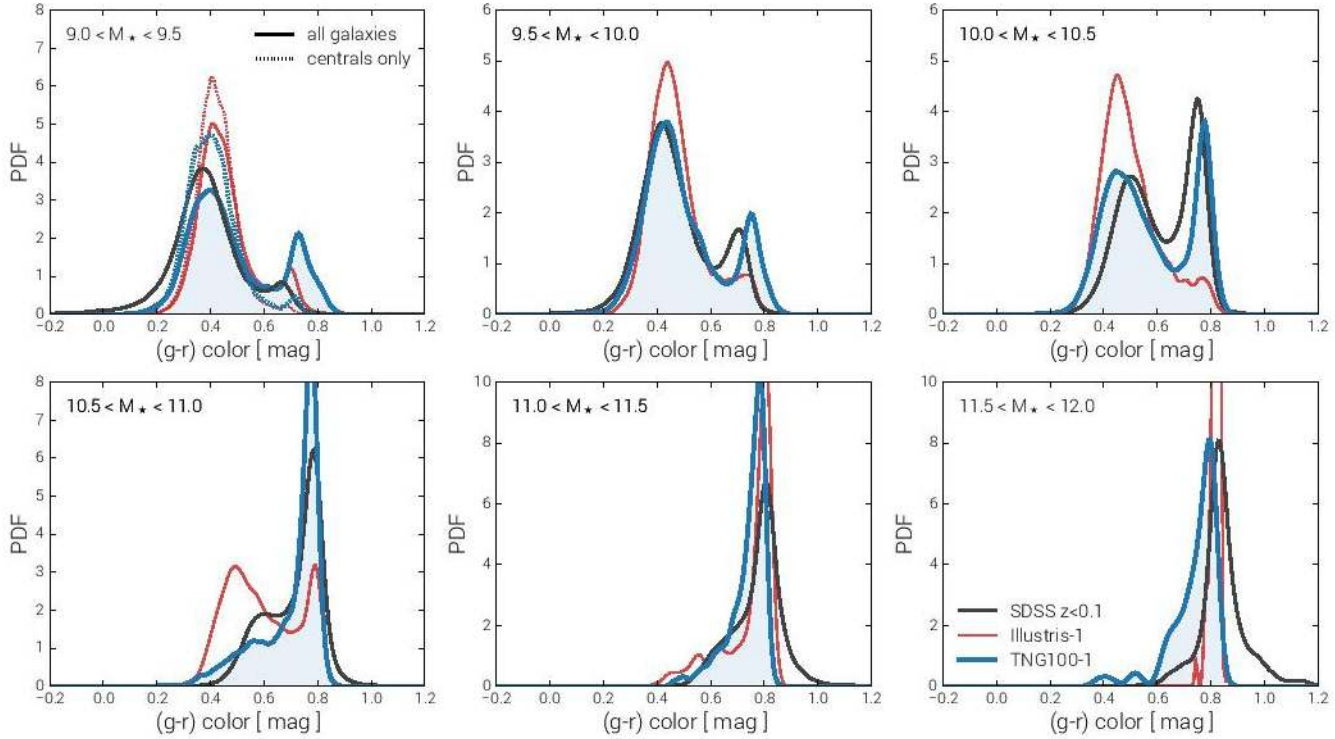

Figure 1. The distribution of simulated versus observed (g-r) colors. In black the SDSS z <0.1 sample is shown, while red shows the result from the old Illustris simulation, and blue the result from our new TNG100 simulation of equivalent box size and resolution. In all cases, galaxies with stellar masses from 10^9 to 10^{12} $M_\odot$ are included, divided into six mass bins as indicated in the six panels. One-dimensional kernel density weighted PDFs are shown. In each case galaxies are shown regardless of if they are centrals or satellites. In addition, in the lowest mass panel we also decompose the simulated results and show

Успехи IllustrisTNG: бимодальность цвета

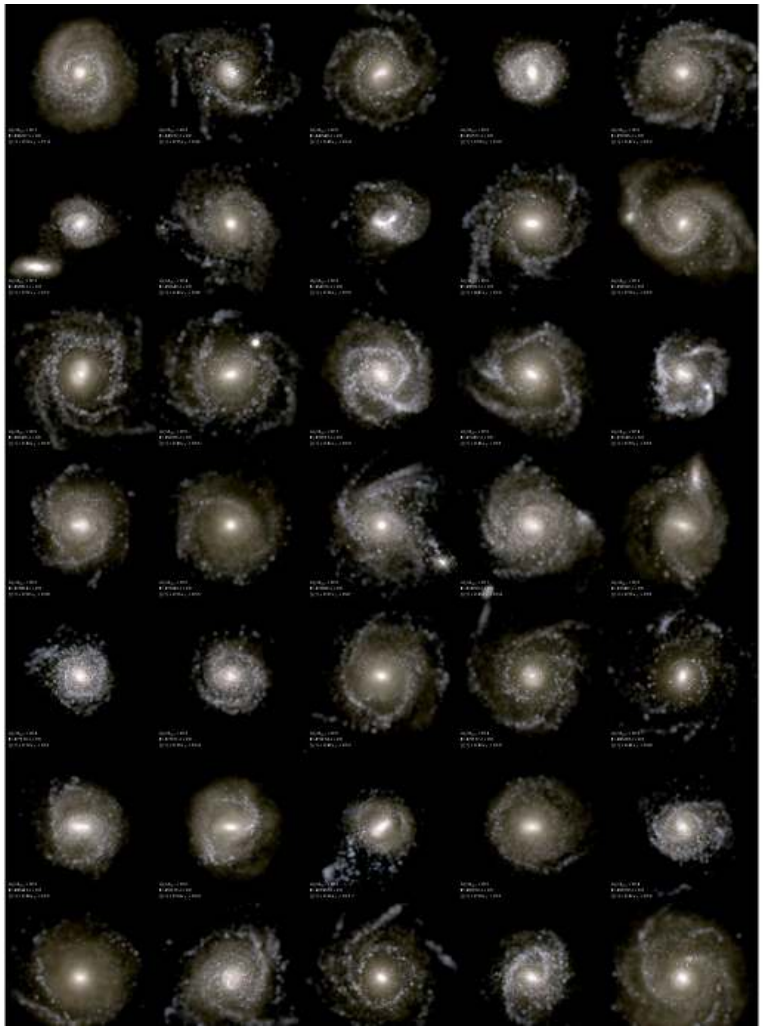

‘Blue’

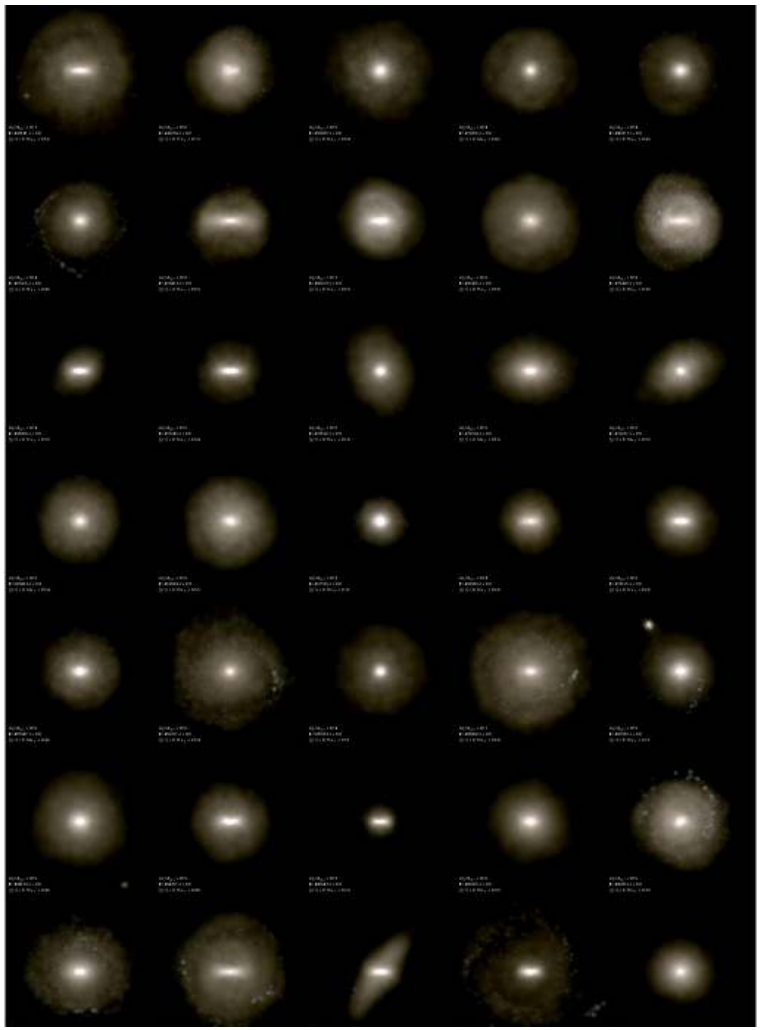

‘Red’

Успехи IllustrisTNG
бимодальность цвета

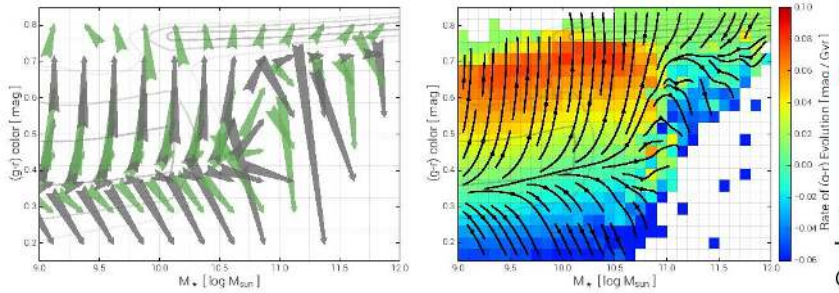

Figure 9. The flux of galaxies across the color-mass plane with time in TNG300-1. Both panels show evolution between $z = 0$ and $z = 0.3$, corresponding to 3.4 Gyr, and include all redshift zero central galaxies. Contours show the locations of the red and blue populations at redshift zero for reference. Left panel individual arrows show the median origin M_* and (g-r) color of all the galaxies which arrive to the indicated bin by $z = 0$. The background grid shows the binning, with green and gray arrows on alternative rows. Right panel: the background color measures the median rate of color evolution, computed from all the galaxies in that bin at redshift zero, in magnitudes per billion years. Overlaid are streamlines (in black) showing the direction of the local vector field $(\partial M_*/\partial t, \partial(g-r)/\partial t)$ of galaxy evolution at that point. Several evolutionary phases are evident including (horizontal) mass growth along the blue population and (vertical) reddening towards quiescence. These figures reveal the dynamic and evolving nature of the color-mass plane by showing the bulk evolution of galaxy ensembles, and do not necessarily represent the pathway of any individual system.

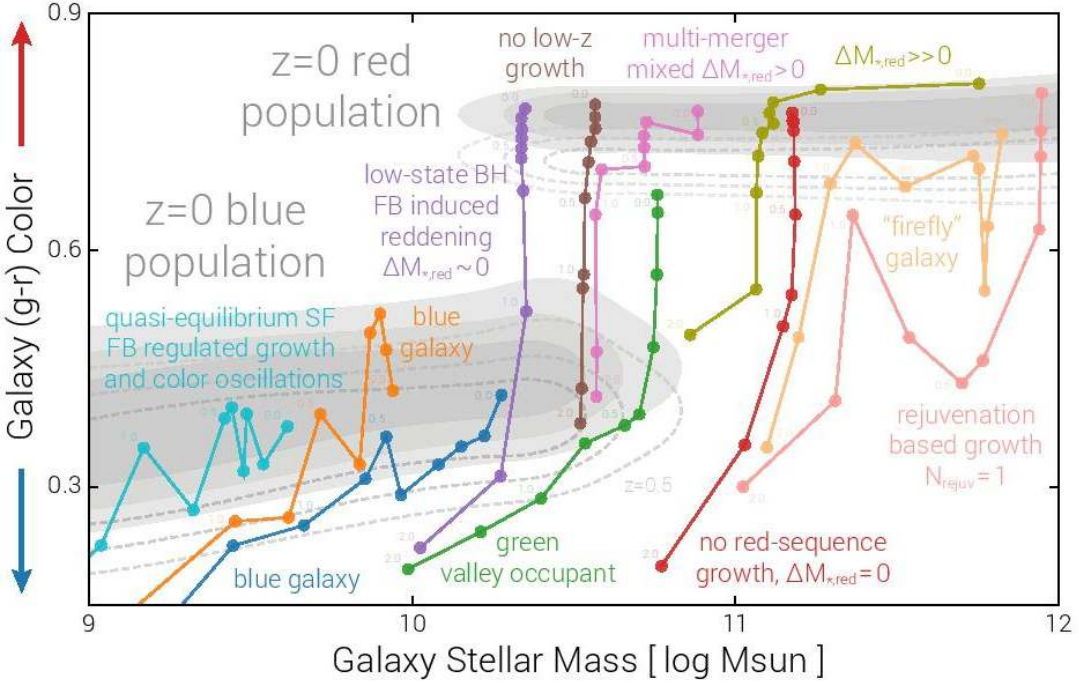

4. Schematic diagram of galaxy evolution across the color-mass plane. The distribution of all $z = 0$ galaxies is shown by the gray co
dotted lines indicate the bulk evolution of the red and blue populations to $z \simeq 0.5$, both moving downward in (g-r). Eleven colored lines
acteristic evolutionary pathways of individual, central galaxies, from at most $z = 2$ to the present day. Although drawn from actual tra

Успехи IllustrisTNG: проблема момента дисков галактик

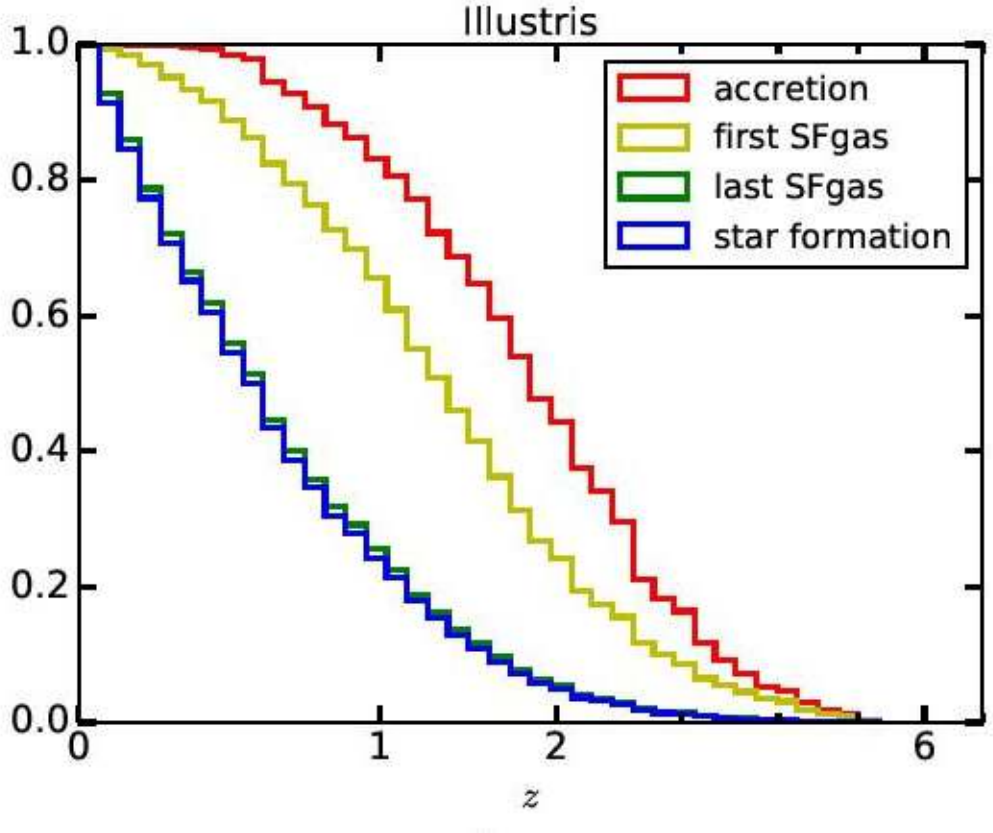

Успехи IllustrisTNG: проблема момента дисков галактик

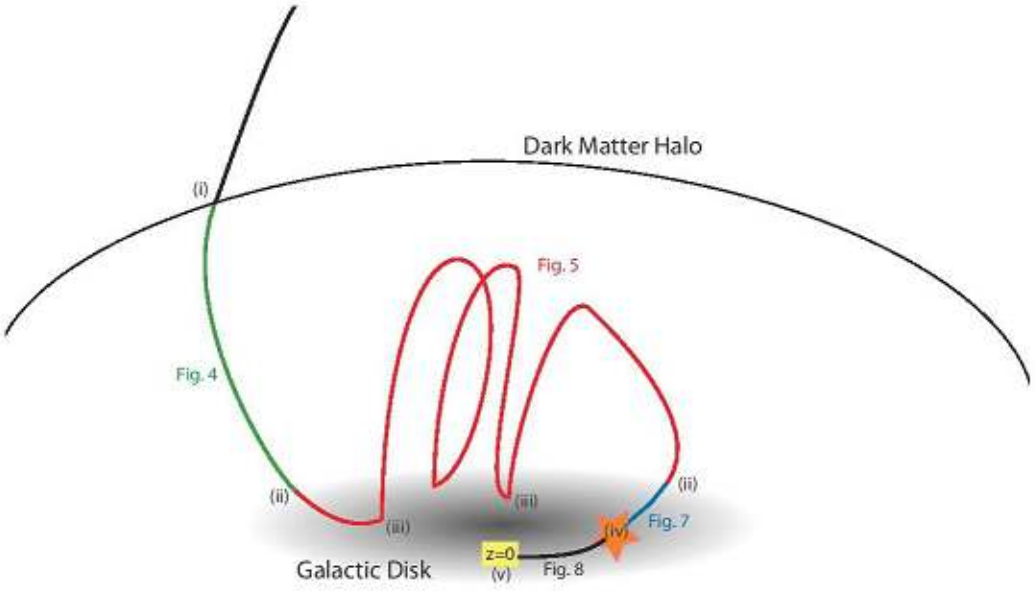

Figure 1. A cartoon illustrating the various 'events' in the evolution of a tracer particle that are considered in this work. These are (i) halo accretion, (ii) first/last becoming part of the star-forming phase, (iii) first/last ejection into the wind, (iv) becoming part of the stellar phase, (v) $z = 0$. In addition, certain intervals between these events that are addressed by particular figures are marked as such.

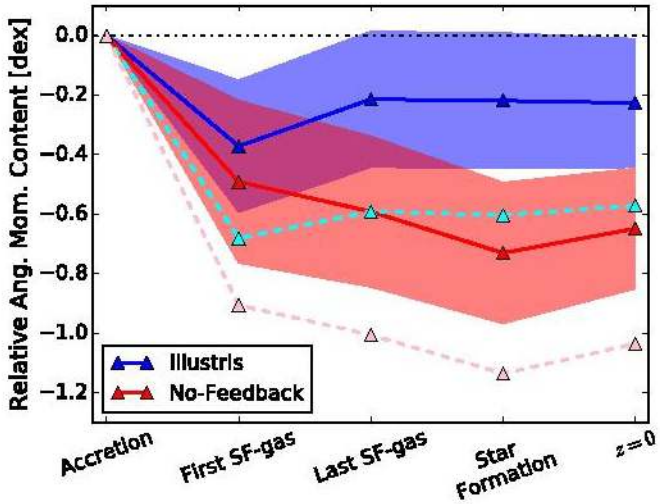

Figure 3. The average angular momentum loss of tracers at events defined in Sec. 2.2 relative to their accretion value for Illustris (blue/cyan) and No-Feedback (red/pink). Solid lines in dark color show the magnitude of the vector sum, while dashed lines in light color show the mean magnitude. The dark-shaded regions are the 1σ spread of relative losses among different galaxies. The 1σ spreads of the relative losses of each individual tracer are ~ 1 dex and are not shown for clarity.

EAGLE+APOSTLE

Simulation	Particle masses ($M_\odot$) DM	Gas	Max softening length (pc)
AP-L3	7.3×10^6	1.5×10^6	711
AP-L2	5.8×10^5	1.2×10^5	307
AP-L1	3.6×10^4	7.4×10^3	134

3.1 The APOSTLE simulations

The APOSTLE[2] simulation suite comprises 12 volumes selected from a large cosmological volume and resimulated using the zoom-in technique (Frenk et al. 1996; Power et al. 2003; Jenkins 2013) with the full hydrodynamics and galaxy formation treatment of the 'Ref' model of the EAGLE project (Schaye et al. 2015; Crain et al. 2015). The regions are selected to resemble the Local Group of galaxies in terms of the mass, separation and kinematics of two haloes analogous to the Milky Way and M 31, and relative isolation from more massive systems. Full details of the simulation setup and target selection are available in Sawala et al. (2015) and Fattahi et al. (2016); we summarize a few key points here.

EAGLE, and by extension APOSTLE, use the pressure-entropy formulation of smoothed particle hydrodynamics (Hopkins 2013) and the numerical methods from the ANARCHY module [Dalla Vecchia et al. (in preparation); see Schaye et al. 2015 for a short summary]. The galaxy formation model includes subgrid recipes for radiative cooling (Wiersma et al. 2009a), star formation (Schaye 2004; Schaye & Dalla Vecchia 2008), stellar and chemical enrichment (Wiersma et al. 2009b), energetic stellar feedback (Dalla Vecchia & Schaye 2012), and cosmic reionization (Haardt & Madau 2001; Wiersma et al. 2009b).

EAGLE+APOSTLE: триаксиальные карлики

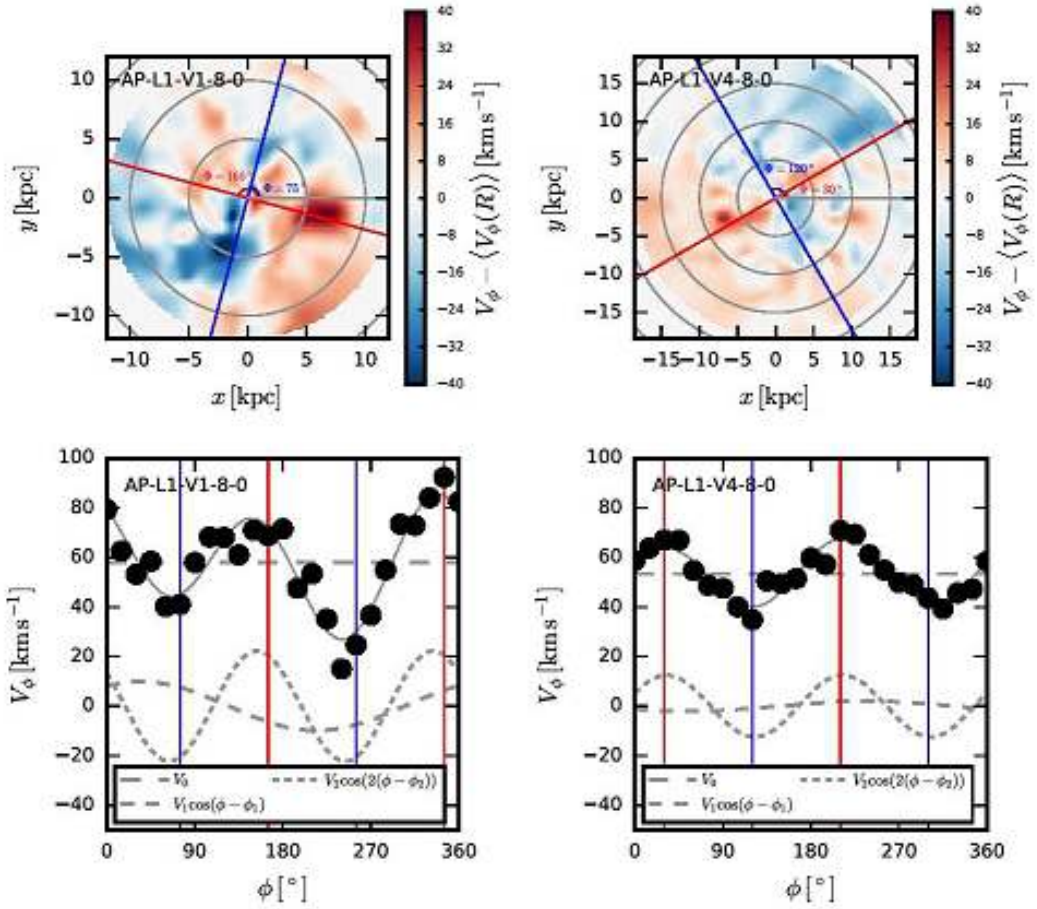

Figure 6. *First row:* Face-on maps of the residual azimuthal motions (after subtracting the mean rotation as a function of radius) in the disc plane for the two galaxies shown in Fig. 5. The red and blue lines correspond to the directions that lie along the major axis of the projections modelled and shown with the lines of corresponding colour in Fig. 5. We label the projection orientation Φ according to its angular offset from the x-axis, as illustrated. The grey circles are drawn at intervals of 5 kpc. *Second row:* Azimuthal velocity at 5 kpc as a function of azimuth (black symbols). The best-fitting first three terms of a Fourier series are shown with broken line styles, the sum of the three with a solid line. The vertical coloured lines correspond to the directions along the lines of the same colours in the upper panels, and coincide approximately with the peaks & troughs of the $m = 2$ mode. This alignment, though imperfect, extends to larger and smaller radii as well.

Marasco:

- Собственно, пытались доказать, что нет cores, а есть некруговое вращение карликов в центре.
- 33 карлика из APOSTLE;
- В центре – триаксиальные! Одинаково в темной материи и в звездах. Скорость вращения узора 1 км/с/кпк, то есть корротация – за пределами галактики.
- Однако заметна третья гармоника. Нашли ее и в галактиках LITTLE THINGS!
- Однако A_3 / A_1 в 2 раза меньше, чем предсказывали симуляции. Что-то не так с триаксиальными гало…

EAGLE+APOSTLE: успехи

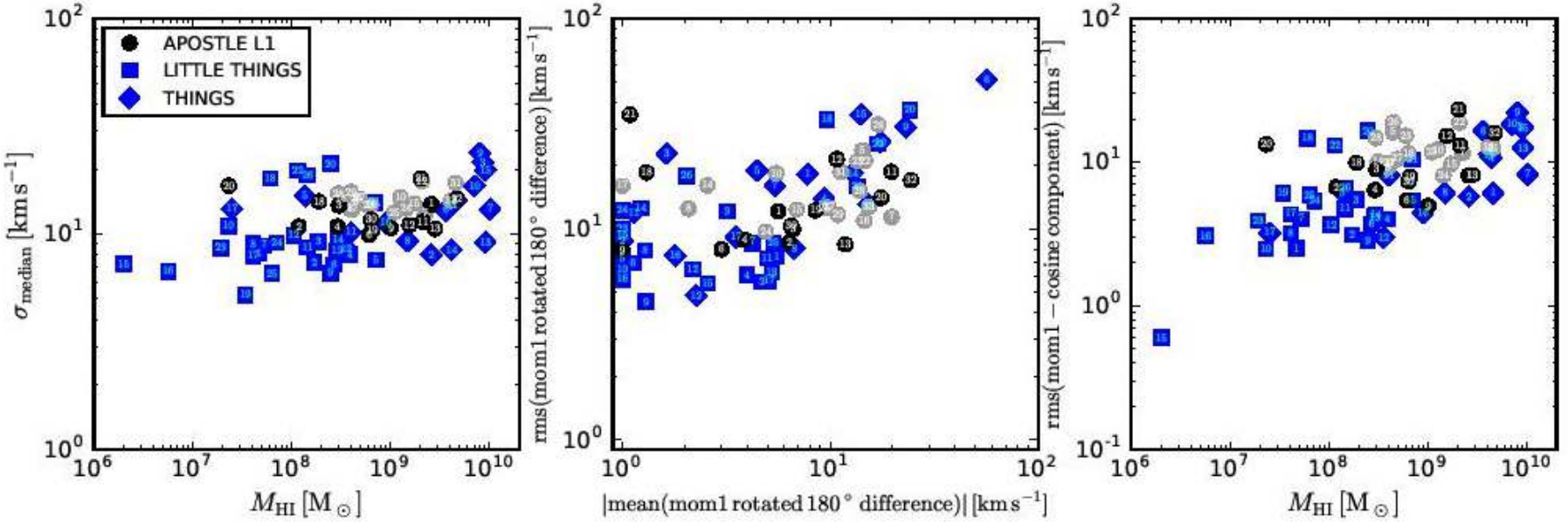

Figure 3. Diagnostics comparing the kinematics of observed and simulated galaxies. In all panels, numbering is as in Fig. 1. *Left:* Median velocity dispersion as measured along the line of sight as a function of H I mass. For the APOSTLE galaxies, the median is calculated across all pixels with $\log_{10}(\Sigma_{\rm HI}/{\rm atoms\,cm^{-2}}) > 19.5$; for the THINGS and LITTLE THINGS galaxies it is computed across all pixels in the S/N masked second moment map. Light grey symbols correspond to galaxies which we flag as kinematically disturbed (see Fig. 4 and Sec. 3.4). *Centre:* As a measure of the symmetry of the velocity field, the first moment (mean velocity field) of each data cube is rotated 180° about its centre and subtracted from itself (with a sign change); here we plot the rms against the absolute mean offset from 0 of the pixels. Pixels which overlap a pixel with no velocity measurement after rotation are discarded. See Fig. B1 and Appendix B for an illustration and further explanation of these measurements. *Right:* The rms about zero of the residual velocity field, derived by subtracting a simple axisymmetric model (Eq. 1) from the original velocity field, as a function of H I mass. See Fig. B2 and Appendix B for an illustration and further explanation of this measurement.

EAGLE+APOSTLE: барионное соотношение Tully-Fisher

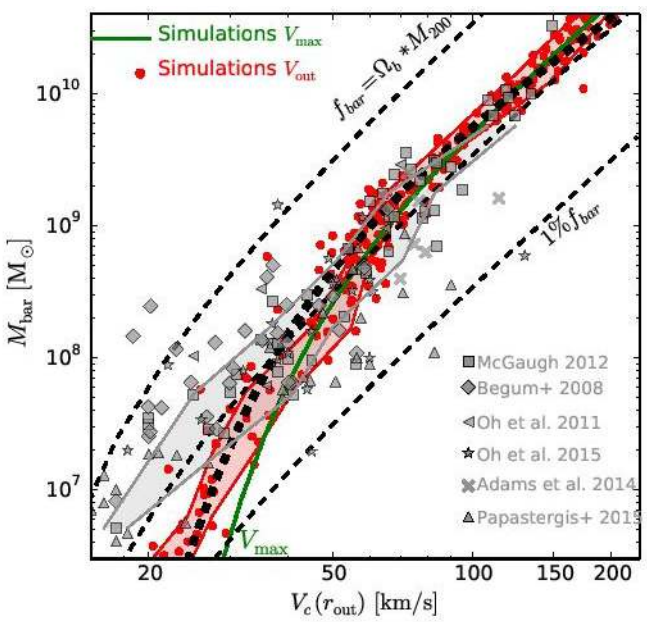

Figure 7. Comparison between predicted and observed baryonic Tully-Fisher relations, extended to include fainter galaxies than in Fig. 4. Grey symbols indicate the observed compilation, from references listed in the legend. Velocities are now defined at r_{out}, the outermost point of the observed rotation curve given in Fig. 6 (or its maximum value, when the two

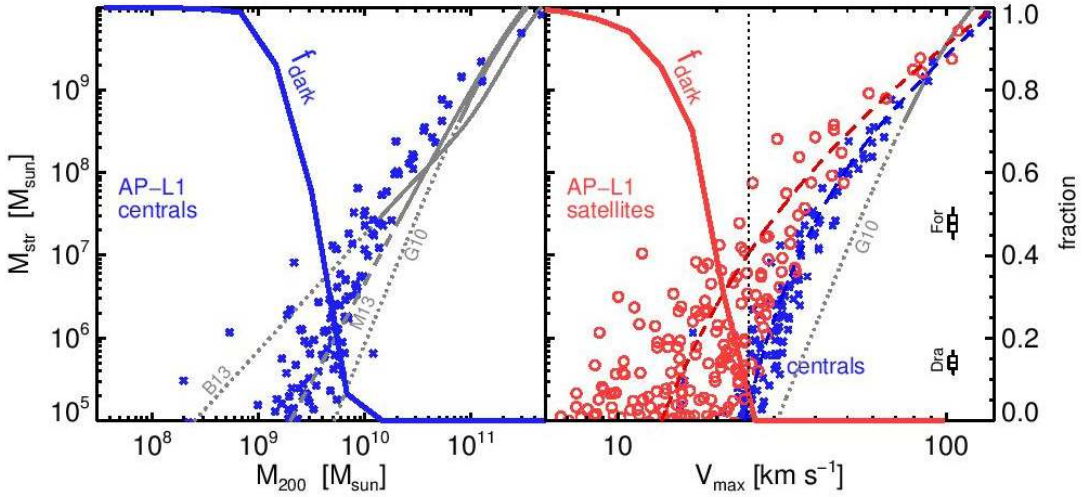

Figure 3. *Left*: Stellar mass – halo mass relation for 'central' galaxies in the highest resolution APOSTLE runs (L1). The abundance matching relations of Guo et al. (2010), Moster et al. (2013) and Behroozi et al. (2013) are shown for reference, labelled as G10, M13, and B13, respectively. The dotted portion of these curves indicates extrapolation of their formulae to low masses. The fraction of 'dark' systems in APOSTLE (i.e., no star particles) as a function of virial mass is indicated by the curve labelled 'f_{dark}', with the scale shown on the right axis. *Right:* Stellar mass versus maximum circular velocity (V_{max}) of centrals and satellite galaxies (at $z = 0$ for both) in APOSTLE, shown as blue crosses and red circles, respectively. The offset between field and satellite galaxies is due to loss of mass, mostly dark matter, caused by tidal stripping. The fraction of 'dark' subhaloes is shown by the solid red curve. There are no dark subhaloes with $V_{max} > 25\,\mathrm{km\ s^{-1}}$. Blue and red dashed lines are fits to the central and satellite stellar mass – V_{max} relations, respectively, of the

Leslie Hunt об успехах Апостола:

- Дисперсия скоростей HI не зависит ни от темпа звездообразования, ни от доли газа (а должна бы, если по Тумре…).
- А вот продолжение барионной зависимости Талли-Фишер до самых маломассивных галактик не удается смоделировать, даже введя стохастический вброс тепловой энергии…

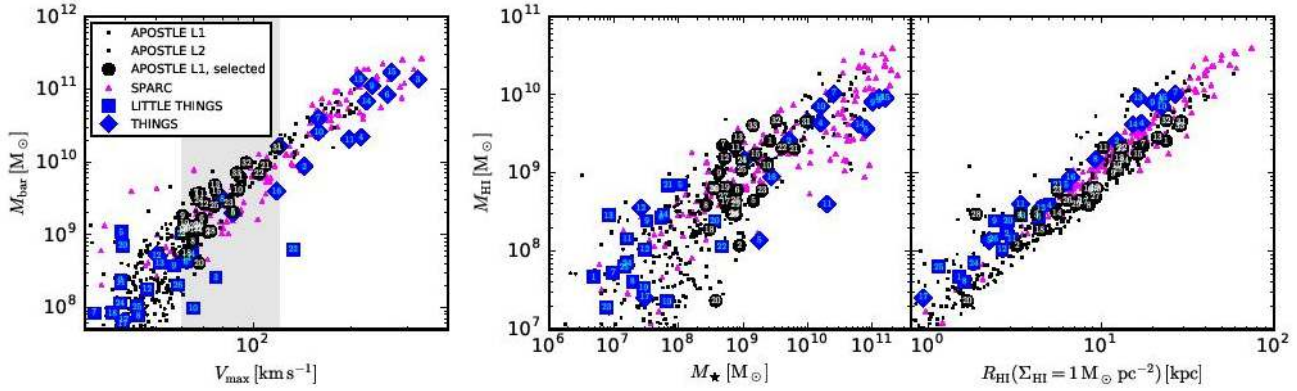

Figure 1. *Left:* Baryonic Tully-Fisher relation (BTFR) for APOSTLE galaxies at resolution AP-L1 (black circles) and AP-L2 (black squares). For comparison we also show the BTFR for the SPARC sample of galaxies (magenta triangles) and the THINGS (blue squares, numbering corresponds to Table A2) and LITTLE THINGS (blue diamonds, see also Table A2) galaxies. In all cases, we assume $M_{\rm gas} = 1.4 M_{\rm HI}$. All AP-L1 galaxies in the range $60 < V_{\rm max}/{\rm km\,s^{-1}} < 120$ (indicated by the gray shaded band) are selected for further analysis and shown with larger, numbered symbols (see Table A1). *Centre:* H I mass – stellar mass relation; symbols and numbering are as in the left panel. *Right:* H I mass–size relation. Sizes are defined as the radius where the H I surface density drops to $1\,{\rm M}_\odot\,{\rm pc}^{-2}$ ($\approx 10^{20}\,{\rm atoms\,cm^{-2}}$). Symbols and numbering are as in the left panel.

Еще новые успешные модели…

- NIHAO от Аарона Даттона (Абудабийский университет)
- Хвастает, что поборол и функцию скоростей Клыпина со товарищи (за счет потери массы карликами+недостаточной протяженность дисков HI+некруговых жвижений+эффектов проекции), и RAR (Radial Acceleration Relation) от Лелли…
- А кстати, о Лелли:

Lelli: обзор SPARC

- 175 кривых вращения с Westerbork'a
- Для этих галактик поверхностная фотометрия Spitzer на 3.6 мкм, переход к плотности через M/L=0.5-0.7…
- И сопоставление g(obs) (~ V^2 /r) versus g(bar) (~M/r^2) вдоль радиуса для каждой галактики!

Lelli: Radial Acceleration Relation

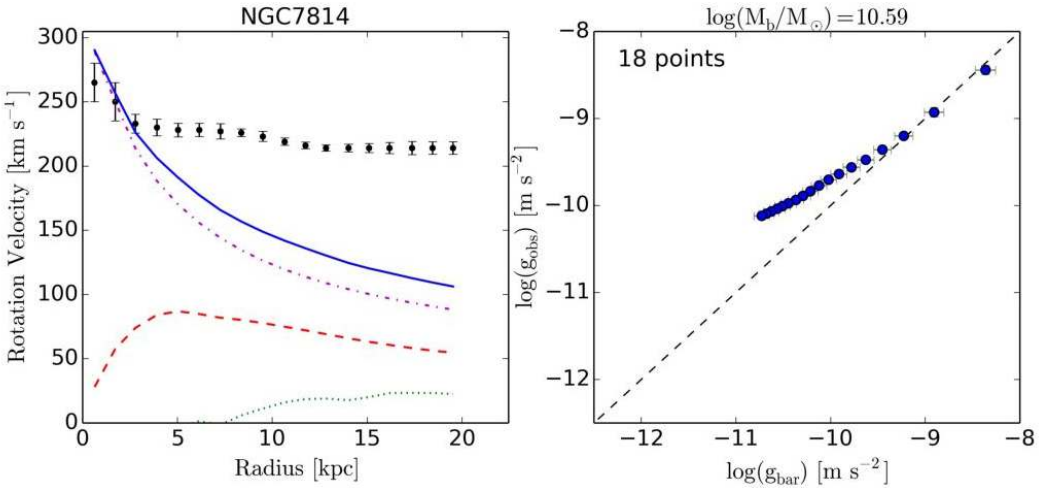

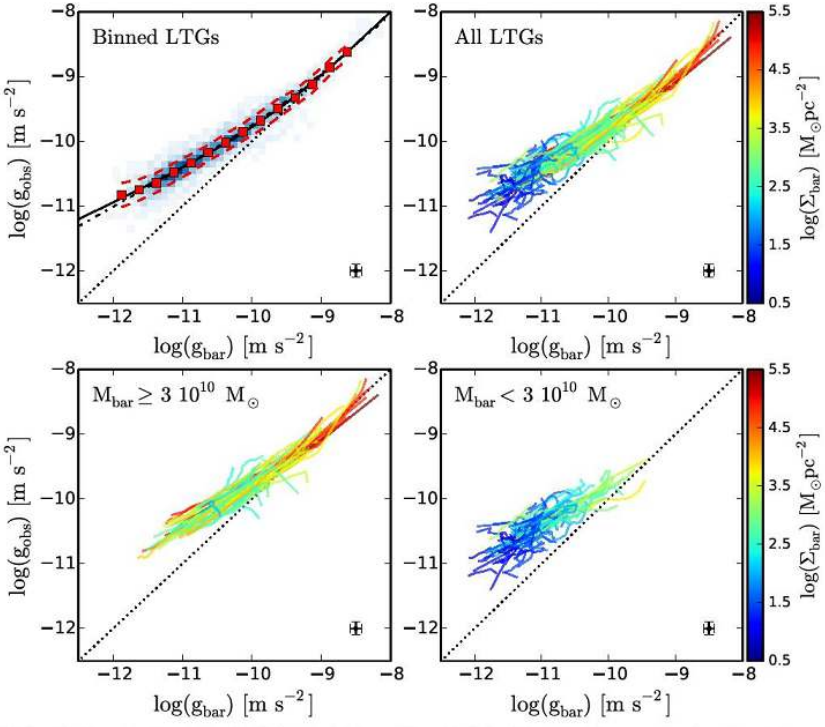

Lelli: Radial Acceleration Relation

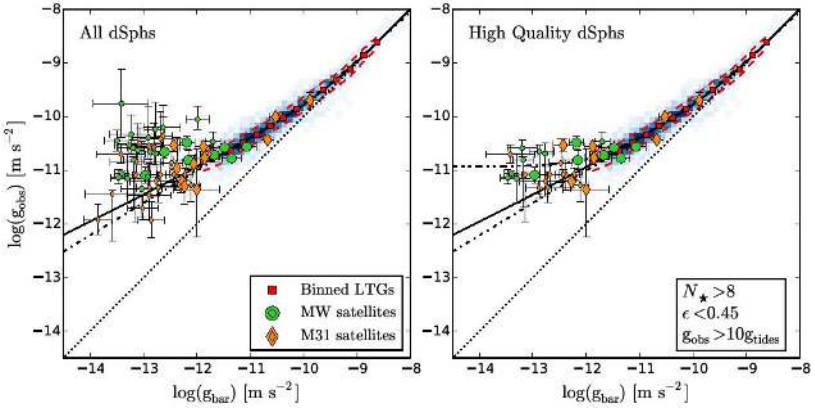

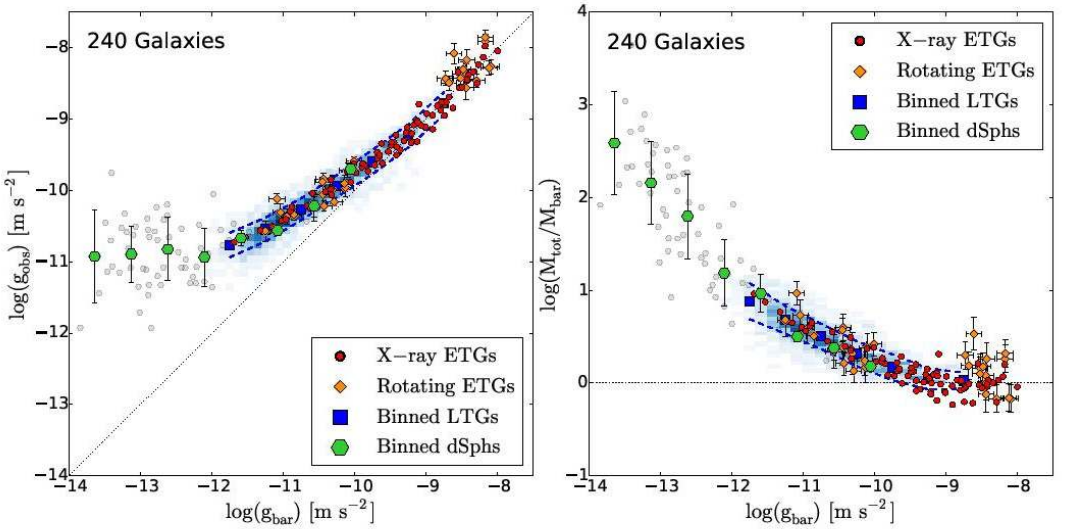

FIG. 12.— Left: The acceleration force relation considering all galaxy types. The colorscale represents ∼2700 points from 153 LTGs: blue squares and dashed lines show the mean and standard deviation of binned data, respectively. Red circles and orange diamonds indicate rotating ETGs and X−ray ETGs, respectively. Small grey hesagons show dSphs: the large green hesagons show the mean and standard deviation of binned data. Right: The mass discrepancy − acceleration relation, where the vertical axis shows $M_{tot}/M_{bar} \simeq g_{obs}/g_{bar}$. This

g(obs)=g(bar)/(1-exp{-sqrt[g(bar)/g(0)]}

Галактики всех типов

Теоретики могут объяснить все! (EAGLE+APOSTLE)

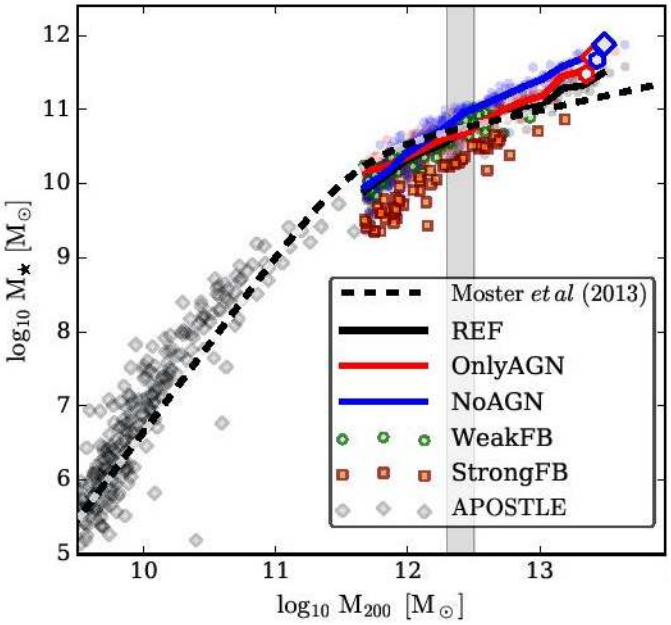

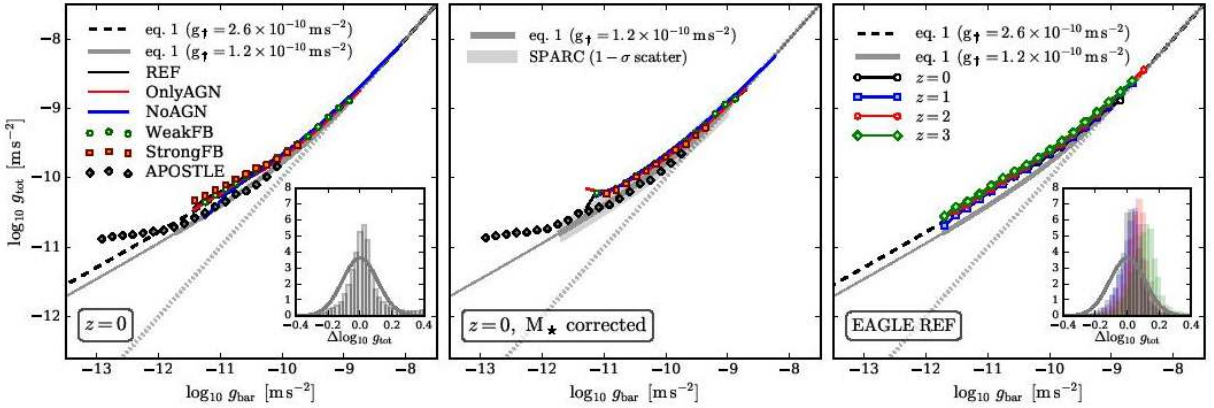

FIG. 3. Total acceleration profiles for all halos as a function of their baryonic acceleration. The left panel shows results for all halos in all simulations at $z = 0$. Lines, points and colors have the same meaning as in Figure 1. The right-hand panel shows (for REF) the redshift evolution for progenitor galaxies. The dashed lines in the left and right-hand panels show eq. 1 with $g_\dagger = 2.6 \times 10^{-10}\,\mathrm{m\,s^{-2}}$. Inset panels show the relative scatter around this curve after combining all simulations (left) and for individual redshifts (right); the solid lines represent the observational scatter in [15]. The middle panel plots the $g_{\rm obs} - g_{\rm bar}$ relation after rescaling galaxy stellar masses so that they fall on the

Ludlow+2016

Наш ответ Чемберлену (Lelli – to APOSTLE)

Recently, Ludlow et al. (2016) analysed simulated galaxies from the EAGLE and APOSTOLE projects. This work significantly increases the statistics and mass range with respect to Santos-Santos et al. (2016) and Keller & Wadsley (2016), but present several problems:

1. Ludlow et al. (2016) fit the simulated data using our Eq. 11 but find $g_\dagger = 3.00$ instead of $g_\dagger = 1.20 \pm 0.02\,(\mathrm{rnd}) \pm 0.24\,(\mathrm{sys})$. The discrepancy is 90σ (rnd) and 7.5σ (sys). This indicates that simulations predict too much DM in galaxies, which is a persistent problem for ΛCDM (e.g., McGaugh et al. 2007; Kuzio de Naray et al. 2009). Indeed, the same simulations were used by the same group to reach the opposite conclusion: many real galaxies show a putative "inner mass deficit" with respect to ΛCDM expectations (Oman et al. 2015).

2. Ludlow et al. (2016) compare the *theoretical* scatter from the numerical simulations with the *observed* scatter. This is not appropriate because the observed scatter is largely driven by observational errors (see Sect. 3.2 and McGaugh et al. 2016). One should compare to the *intrinsic* scatter, which is either zero or extremely small ($\lesssim$0.05 dex). The theoretical scatter from Ludlow et al. (2016), though small (0.09 dex), is still too large compared to the observations.

3. Ludlow et al. (2016) compute g_{obs} and g_{bar} assuming spherical symmetry instead of estimating the gravitational potential in the disk mid-plane. The difference between spherical and disk geometry is not terribly large but significant. This introduces systematics that are hard to address.

4. According to their Figure 3 (left panel), there is a systematic off-set between high-mass galaxies from EAGLE and low-mass galaxies from APOSTOLE. We do not observe any off-set between high and low mass galaxies (see Fig. 3 and Fig. 5).